RSC Advances

PAPER

View Article Online
View Journal | View Issue

Cite this: *RSC Adv.*, 2020, **10**, 9438

Preparation and electrochemical properties of nanostructured porous spherical $NiCo_2O_4$ materials

Chunyang Li,[ac] Yan Liu,[ab] Guojun Li *[ab] and Ruiming Ren[b]

Porous spherical $NiCo_2O_4$ powders with a micro–nano structure were prepared by the spray drying method using citric acid as the chelating agent and soluble salts as cobalt and nickel sources. By calcination at 300 °C, spherical and single-phase spinel-type $NiCo_2O_4$ powders were obtained. The powders with particle sizes of 0.5–3 μm were aggregations of nano-sized grains (about 15–30 nm). The electrical property tests demonstrated that the synthesized $NiCo_2O_4$ has a specific capacitance of 430.67 F g^{-1} at a current density of 1 A g^{-1} and a capacitance retention rate of 100% after 3000 cycles at a current density of 4 A g^{-1}, indicating excellent cycling stability. On assembly into an asymmetric supercapacitor device, a specific capacitance of 37.06 F g^{-1} and energy density of 13.18 W h kg^{-1} at a power density of 800 W kg^{-1} and a current density of 1 A g^{-1} were demonstrated. The micro–nano structured porous $NiCo_2O_4$ powders have a larger specific surface area, which can allow the sample to come in full contact with the electrolyte. The nanopore channels are favourable for releasing the lattice distortion stress during the charge–discharge process, maintaining the structural stability of the crystal and improving the cycle life.

Received 10th January 2020
Accepted 15th February 2020

DOI: 10.1039/d0ra00259c

rsc.li/rsc-advances

Introduction

Supercapacitors have been widely used in many fields by virtue of their advantages such as high power density, rapid charge and discharge and excellent cycling stability.[1] Based on the energy storage mechanism, the fast and reversible redox reaction of a pseudocapacitor leads to higher specific capacity than that of an electric double-layer capacitor.[2,3] Thus, the study of pseudocapacitor materials has become a hot topic in the field of energy storage. Among the materials studied, such as RuO_2, NiO, MnO_2, and Co_3O_4, spinel $NiCo_2O_4$ is considered to be one of the most promising materials for supercapacitors due to its high specific capacitance, excellent cycling stability, low cost and environmental friendliness.[4–7] However, at high current densities, the relatively low conductivity, cycling stability and poor rate performance have restricted the practical application of $NiCo_2O_4$.[8]

At present, the research on the single-phase $NiCo_2O_4$ materials mainly focuses on the preparation of special micromorphology to increase the specific surface area and then improve the electrochemical performance.[9–15] The nanorods, nanowires, nanosheets and urchin-like particles of $NiCo_2O_4$ were prepared on a Ni foam network, and they exhibited better specific capacitance, energy density and cycling stability.[9–15] However the above-mentioned synthesis reactions were carried out on a Ni foam or carbon fabric substrate in solution and there is a high demand for equipment; thus, the substrates may be contaminated and mass production is also not easy to achieve. Currently, mass production methods, such as co-precipitation[16] and sol–gel,[17] are suitable for preparing $NiCo_2O_4$ nanoparticles, but the synthesized nanoparticles without special morphology are easy to agglomerate and their electrochemical performances are relatively poor; even a small number of mono-dispersed nanoparticles may pass through the separator and cause a short circuit. In general, the nano-structured $NiCo_2O_4$ is advantageous for increasing specific capacitance and energy density due to the increase in its specific surface area and the short diffusion path of the charge.[18] In addition, it has been proved that the channels of the porous electrode materials can make charge transfer fast and enhance the high rate charge–discharge performance.[19,20] Based on the above-mentioned summary and analysis, it is necessary to develop a low-cost method for preparing a porous $NiCo_2O_4$ material with special morphology. In recent years, the authors have successfully prepared spherical porous $Li_4Ti_5O_{12}$ and $LiFePO_4$/C materials with a micro–nano structure by a low-cost, continuous and mass production spray drying technology. The as-obtained materials showed excellent electrochemical performance and cycle life.[21,22] Therefore, the objective of this article is to use

[a]*Liaoning Key Lab for New Energy Batteries, Dalian Jiaotong University, Dalian 116028, China*

[b]*School of Materials Science and Engineering, Dalian Jiaotong University, Dalian 116028, China. E-mail: guojunlee@163.com*

[c]*School of Environmental and Chemical Engineering, Dalian Jiaotong University, Dalian, 116028, China*

a low-cost, continuous, mass production spray drying technology to synthesize spherical, porous $NiCo_2O_4$ materials with special micro–nano structures and achieve good electrochemical performance.

In this work, the solid, micro–nano structured spherical porous $NiCo_2O_4$ powders were prepared by a spray-drying process using citric acid as the chelating agent and soluble salts as cobalt and nickel sources. The microstructure, phase and electrochemical properties of the samples obtained were investigated.

Experimental

Preparation of samples

$Ni(CH_3COOH)_2 \cdot 4H_2O$, $Co(CH_3COOH)_2 \cdot 4H_2O$ and $C_6H_8O_7 \cdot H_2O$ (citric acid) in a molar ratio of 1 : 2 : 3 were completely dissolved in 50 mL deionized water and then the pH of the obtained solution was adjusted to 8.0–8.5 by aqueous ammonia. Finally, the above-mixed solution was placed in a forced-air oven at 150 °C for 14 h to obtain a chelated purple solid. The product obtained was dissolved using ammonia in 100 mL deionized water and 50 mL $C_4H_{10}O_2$ (ethylene glycol ether) was added in. The spherical $NiCo_2O_4$ precursor was obtained by spray-drying the solution at a temperature of 150 °C, pressure of 0.3 MPa, and a feeding rate of 550 mL h^{-1}. The spherical porous $NiCo_2O_4$ with a micro–nano structure was prepared by calcination of the spherical $NiCo_2O_4$ precursor at 250–500 °C for 4 h in air.

Physical characterization

X-ray diffraction (XRD, Empyrean with Cu-Kα radiation), transmission electron microscopy (TEM, JEM 2100F, Japan) and scanning electron microscopy (SEM, SUPRA 55) were used to study the phase structure and morphology of the sample, respectively. The N_2 adsorption and desorption test (BET, Quantachrome 3SI-MP-11) method was employed to determine the surface area and pore size of the sample. X-ray photoelectron spectroscopy (XPS, PHI 5700) was used to analyze the surface element content of the sample.

Electrochemical measurements

The working electrode was prepared by mixing and dispersing 80 wt% active material, 10 wt% acetylene black and 10 wt% polyvinylidene fluoride (PVDF) in 1-methyl-2-pyrrolidone (NMP). The mixed slurry was coated on 1 cm^2 of cleaned foamed nickel and dried in a vacuum at 110 °C for over 12 h. The mass of the active substance on the electrode was approximately 1 mg. In the three-electrode electrochemical tests at the electrochemical workstation (CHI600B, Shanghai, China), a saturated calomel electrode (SCE) was used as the reference electrode, a platinum electrode was used as the counter electrode, and 2 M KOH was used as the electrolyte. An asymmetric supercapacitor was assembled, with the active material as the positive electrode material, activated carbon as the negative electrode material, and glass fibre as the separator, and tested on the Neware Battery Testing System (CT-S4, Guangdong, China).

Results and discussion

Material characterization

Fig. 1 shows the XRD patterns of the obtained samples at the different temperatures. It was observed that the obtained precursor and sample calcined at 250 °C were amorphous due to the existence of no obvious diffraction peak (Fig. 1a and b), showing no $NiCo_2O_4$ crystal obtained below 250 °C. When the calcination temperatures were between 300 °C and 400 °C, the amorphous precursor crystallized into a single-phased spinel-type $NiCo_2O_4$ (Fig. 1c–e). The diffraction pattern of the calcined sample was completely consistent with the $NiCo_2O_4$ diffraction pattern (JCPDS: 73-1702), while the strong X-ray diffraction characteristic peaks observed at 30.9°, 36.4°, 44.2°, 58.8°and 64.7° correspond to the (220), (311), (400), (511) and (440) crystal faces, respectively. When temperatures were greater than 450 °C, the spinel-type $NiCo_2O_4$ decomposed into spinel-type Co_3O_4 and NiO, indicating that the spinel type $NiCo_2O_4$ is metastable since the strong redox reactions of Co^{3+}/Co^{2+} and Ni^{3+}/Ni^{2+} cause structural changes in $NiCo_2O_4$ above a certain temperature.[23] This phenomenon agrees well with the research results.[24,25] According to the Scherrer formula (*i.e.* $D = 0.89\lambda/(\beta \cos \theta)$), detailed peak broadening analysis of the (311) XRD reflection indicates that the average grain size of the obtained $NiCo_2O_4$ samples can be estimated to be ~15, ~21 and ~24 nm at 300, 350, and 400 °C, respectively, showing that the grain size gradually becomes larger on increasing the calcination temperatures. Because the bigger grains are not conducive to improving the electrochemical performance, the calcination temperature of 300 °C was selected.

Figure 2 shows the microstructure of the precursor and the sample obtained at 300 °C. It can be seen from Fig. 2a that the precursor with the particle size of 1–5 μm is spherical and relatively smooth. In contrast to the precursor, the particle size of the sample calcined at 300 °C was remarkably reduced to 0.5–2 μm, and small pores were observed on the surface of the particles. As observed from the cross-sectional views of the calcined sample (Fig. 2c and d), the spherical particles were aggregated from nano-sized grains (15–30 nm) with

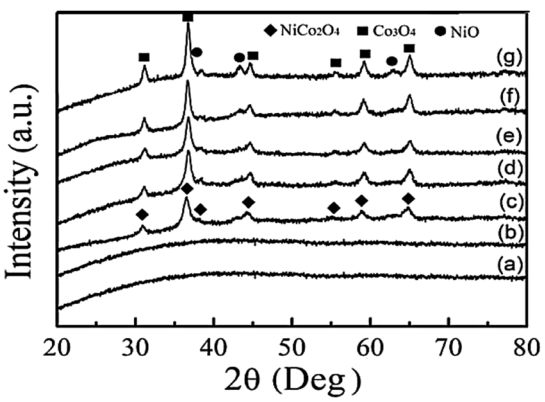

Fig. 1 XRD patterns of the obtained samples at different temperatures. (a) The precursor, (b) at 250 °C (c) 300 °C (d) 350 °C (e) 400 °C (f) 450 °C (g) 500 °C.

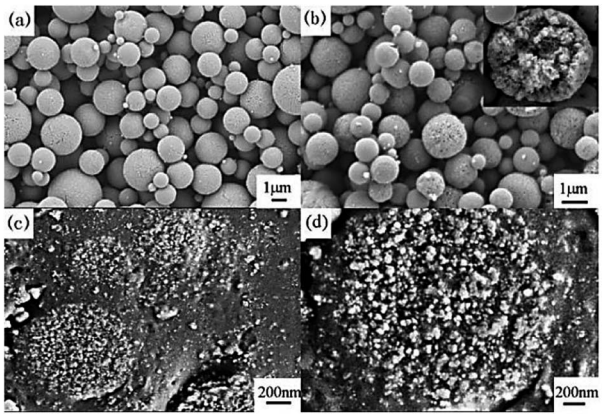

Fig. 2 FE-SEM images of $NiCo_2O_4$ obtained at 300 °C. (a) Precursor, (b) calcined sample, (c) and (d) the cross-section at different magnifications.

interconnected pores between these grains. This is because the citrate and residual acetate decomposed to gas and then cause the dense precursor spheres to vacate during the calcination process. After reaching a certain temperature, the $NiCo_2O_4$ nanocrystals began to form and a large amount of the nanocrystals slowly grew and aggregated in the sphere to form microspheres with a porous structure and, finally, a single-phase $NiCo_2O_4$ spherical powder with a micro–nano porous structure was obtained.

Fig. 3 shows the TEM images and SAED pattern of the $NiCo_2O_4$ calcined at 300 °C. It can be clearly seen from the images (Fig. 3a–c) that there are voids in the $NiCo_2O_4$ microspheres, indicating that the particles inside have lots of nanopores. These voids can store electrolytes and promote ion exchange between the electrolyte and electrode material, resulting in an improved electrochemical performance.[26] The SAED pattern (Fig. 3d) shows an obvious polycrystalline diffraction aura, which indicates that $NiCo_2O_4$ is polycrystalline. By indexing to the *Fd3m* space group of the spinel $NiCo_2O_4$ cube, the crystal surfaces were labeled as (311) (400) and (440), respectively.

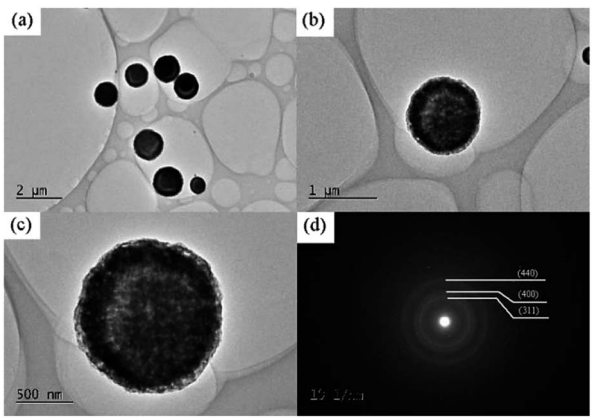

Fig. 3 (a)–(c) TEM images of different magnifications and (d) the SAED pattern of the calcined $NiCo_2O_4$.

Fig. 4 shows the specific surface area and pore diameter distributions of the $NiCo_2O_4$ powder obtained at 300 °C. Fig. 4a shows that the N_2 adsorption-curve of the sample is the IV type, indicating the presence of micropores or mesopores. It can be seen from Fig. 4b that the pore structure does exist in the sample particles. The specific surface area of $NiCo_2O_4$ powder is 42.17 m^2 g^{-1}, and the pore diameter is concentrated in 5–30 nm, with an average of 4.233 nm. The nano-sized pores are conducive to increasing the specific surface area so that sites are available for increased electron conduction in $NiCo_2O_4$.

Fig. 5 shows the XPS spectra of the surface of the calcined $NiCo_2O_4$. The survey spectrum (Fig. 5a) indicates the presence of Ni, Co, and O, as well as C based on the reference and the absence of other impurities. By using the Gaussian fitting method, the Ni 2p emission spectrum (Fig. 5b) exhibits two spin–orbit bimodal emission peaks, namely Ni^{2+} and Ni^{3+} and two shake-up satellite peaks ("sat."). The binding energies at 854.79 eV and 871.62 eV belong to Ni^{2+}, and the binding energies at 855.36 eV and 873.32 eV belong to Ni^{3+}.[27] The Co 2p spectrum (Fig. 5c) are well fitted with two spin–orbit doublet peaks characteristic of Co^{2+} and Co^{3+} and two shake-up satellite peaks. The peaks with binding energies of 781.10 eV and 796.86 eV were derived from Co^{2+}, and those at 779.56 eV and 794.82 eV are ascribed to Co^{3+}.[28] As shown in Fig. 5d, the O 1s spectrum shows three oxygen-donating groups. O 1(529.54 eV) is a typical metal–oxygen bond, O 2(531.8 eV) corresponds to a defect site of low oxygen-coordination in small-sized particles,

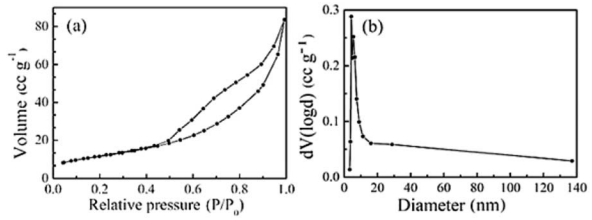

Fig. 4 N_2 adsorption and desorption isotherms of the samples obtained at 300 °C. (a) Specific surface area (BET) (b) pore-size distribution (BJH).

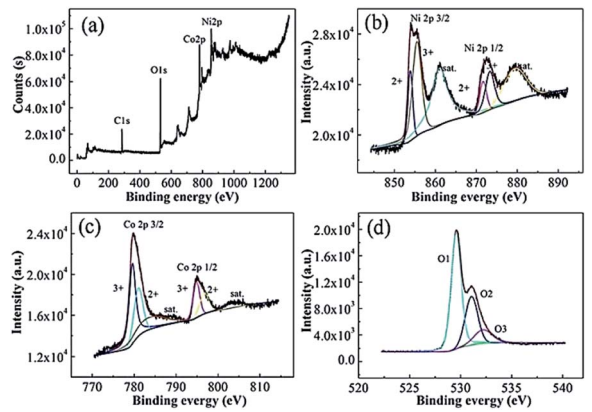

Fig. 5 XPS spectra of (a) the calcined $NiCo_2O_4$ powder, (b) Ni 2p, (c) Co 2p, (d) O 1s.

and O 3(532.2 eV) may be a variety of physically and chemically adsorbed waters on and within the surface.[29] These results show that the chemical composition of porous $NiCo_2O_4$ microspheres includes Co^{2+}, Co^{3+}, Ni^{2+}, and Ni^{3+}, which is in good agreement with the results in the literature for $NiCo_2O_4$.[30,31]

Investigation of electrochemical performances

Fig. 6a shows the cyclic voltammetry (CV) curves of $NiCo_2O_4$ at a scan rate of 5–100 mV s^{-1}. Compared with electric double-layer capacitance characterized by nearly rectangular CV,[29] the shapes of the CV curves clearly confirm the pseudo-capacitive behavior. Unlike the blank nickel foam, a pair of redox peaks were observed within 0 to 0.5 V, indicating that the charge storage was achieved by $NiCo_2O_4$ loaded on the nickel foam surface by faradaic redox reactions of Co^{2+}/Co^{3+} and Ni^{2+}/Ni^{3+}. The redox reaction is expressed as eqn (1).[32,33]

$$NiCo_2O_4 + OH^- + H_2O \leftrightarrow NiOOH + 2CoOOH + 2e^- \quad (1)$$

As the scan rate increased, the area of the CV curve increased and the position of the cathodic peak shifted from 0.22 to 0.15 V, indicating the low resistance of the electrode because of the conductive Ni substrate. Fig. 6b shows the galvanostatic charge and discharge curves of the sample in the 0–0.45 V range at different current densities. Distinctly, the existence of plateaus at around 0.25 V suggests an ideal pseudocapacitance, which is in good agreement with the CV curves (Fig. 6a). The specific capacitance was calculated according to eqn (2):

$$C_s = I\Delta t/m\Delta V \quad (2)$$

where C_s (F g^{-1}) refers to the specific capacitance, I (A) refers to the discharge current, Δt (s) refers to the discharge time, ΔV (V) refers to the potential change during discharge and m (g) refers to the mass of the active material. The specific capacitances at current densities of 1, 2, 4, 6, 8 and 10 A g^{-1} are 432.67, 412.89, 387.56, 358.67, 337.78 and 317.78 F g^{-1}, respectively. As the current density increases, the specific capacitance decreases. When the current density was 10 A g^{-1}, the specific capacitance was equivalent to 74% of the initial capacitance, indicating the high specific capacitance and good rate characteristics of the prepared micro–nano porous spherical $NiCo_2O_4$ electrode. Fig. 6c shows the electrochemical impedance spectra (EIS) of the $NiCo_2O_4$ and fitting plot of the equivalent circuit. As observed, the equivalent circuit consists of R_s, R_{ct}, Z_W, C_{dl} and CPE_{PC}.[34] R_s represents the mass transfer resistance and contact resistance, which is reflected by the intercept of the curve and the real axis in high-frequency regions.[35,36] R_{ct} refers to the charge transfer resistance caused by the faradaic reactions, which is reflected by the diameter of the semicircle in the medium-to-high frequency region. Representing the ion diffusion resistance inside the active material particles, the Warburg impedance Z_W is reflected by the oblique line in the low-frequency region. C_{dl} refers to the electric double-layer capacitance on the electrode materials[35] and CPE_{PC} represents the constant phase element. In contrast with the results in the literature,[36,37] the obtained sample with an R_{ct} value of 0.71 Ω is lower or similar, which is advantageous for the rapid transfer of charge. Fig. 6d illustrates the cycle life curve and partial charge and discharge curves of the $NiCo_2O_4$ electrode. The specific capacitance was 398.22 F g^{-1} after 3000 cycles at a current density of 4 A g^{-1}, and the capacitance retention rate was 100%, indicating excellent stability. For the first 1000 cycles, the specific capacity increased even more, caused by the activation process of the electrode material. After a continuous charge–discharge process, more contact sites were activated, and the specific capacitance obviously increased. It can be seen from the partial charge–discharge curve that the curve has good symmetry and stability, indicating that the material structure of the test process is relatively stable. The spherical $NiCo_2O_4$ powders have considerable micro–nano pores, which optimize their contact with the electrolyte. As a result, the adsorption–desorption rates of ions were enhanced, the diffusion resistance was reduced, the structural stability of the crystal was maintained better, the lattice distortion effect caused by the charge–discharge process was eliminated, and the service life was extended.[21]

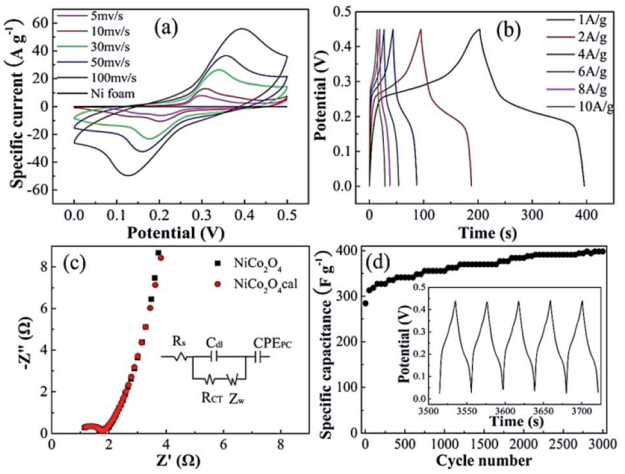

Fig. 6 (a) CV curves of $NiCo_2O_4$ at different scan rates. (b) Charge–discharge curves of different current densities of $NiCo_2O_4$ in 0–0.45 V. (c) EIS of the $NiCo_2O_4$ and fitting plot of the equivalent circuit. (d) Cycle life curve and partial charge–discharge curve of $NiCo_2O_4$.

Fig. 7a shows the CV curve of the positive and negative materials at a sweep speed of 10 mV s^{-1}. By using the specific electricity calculation formula, it was found that the mass ratio of the positive and negative electrodes was about 0.8 : 1. Fig. 7b shows the CV curves for different scan rates of $NiCo_2O_4$//AC, where it can be seen that the potential window is significantly expanded to 1.7 V and the shape of the curve is different from that of the electric double-layer and pseudocapacitor. On increasing the scanning rate, the response current increased accordingly and the shape of the curve remained good, indicating good dynamic performance. Fig. 7c shows the charge–discharge curves at different current densities. The assembled supercapacitor achieved the purpose of expanding the voltage window and obtaining higher power and it was observed that each curve exhibited good symmetry at a higher current density.

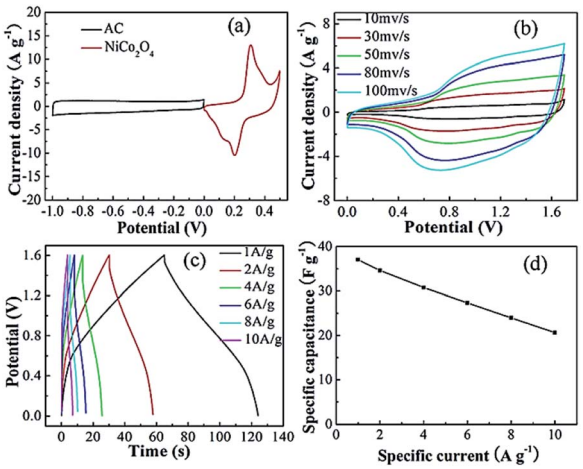

Fig. 7 (a) The CV curve of the positive and negative materials at a sweep speed of 10 mV s^{-1}. (b) CV curves at different scan rates, (c) the charge–discharge curves and (d) specific capacity comparison curves at different current densities.

There is no obvious voltage drop, which indicates that the characteristics of the pseudocapacitance capacitor are still dominant after it is assembled into an asymmetric supercapacitor, which has ideal capacitive behavior, high coulombic efficiency and excellent electrical conductivity. Fig. 7d is a comparison of the specific capacities at different current densities. The specific capacitances at the current densities of 1, 2, 4, 6, 8 and 10 A g^{-1} were calculated by eqn (2) to be 37.06, 34.63 30.75, 27.37, 24, and 20.63 F g^{-1}, respectively. In contrast to the capacity at 1 A g^{-1}, the capacity retention rate at 10 A g^{-1} is 55.7%, indicating that the assembled capacitors exhibit better electrochemical performance. Subsequently, further cyclic life tests are needed to observe the structural stability of pseudocapacitive electrode materials.

Fig. 8a shows the calculation results of the power density and energy density of the assembled supercapacitor according to formulas (3) and (4).

$$E = C_s \Delta V^2/2 \quad (3)$$

$$P = E/t \quad (4)$$

C_s is the specific capacitance (F g^{-1}), ΔV is the potential change (V) during discharge, E is the energy density (W h kg^{-1}), P is the power density (W kg^{-1}), and t is the discharge time (s). The $NiCo_2O_4$//AC supercapacitor has an energy density of 13.18 W h kg^{-1} at a power density of 0.8 kW kg^{-1}, which is higher as compared to other studies, such as GO/CoAl-LDH (6 W h kg^{-1} at 1.5 kW kg^{-1}),[38] GF/CNT/MnO_2-GF/CNT/Ppy (6.2 W h kg^{-1} at 2.7 kW kg^{-1}),[39] Cu/CuO_x@$NiCo_2O_4$//AG (12.6 W h kg^{-1} at 0.344 kW kg^{-1}).[12] The cycle life test that was performed on the assembled $NiCo_2O_4$//AC capacitor is shown in Fig. 8b. The capacity has a significant rise in the initial pre-cycle due to sufficient activation between the electrode material and the electrolyte. After 12 000 cycles at a current density of 4 A g^{-1}, the capacitance retention was 100%, suggesting its excellent cycling stability.

The above results indicate that the spherical porous $NiCo_2O_4$ electrode material with micro–nano structure is beneficial for exhibiting the pseudocapacitor characteristics, diffusion and transfer of charges and increase in the structural stability and cycle life during the charge–discharge process.

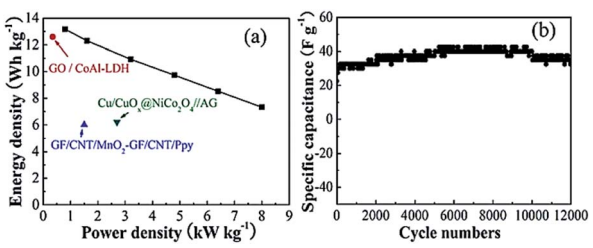

Fig. 8 Curves of (a) power-energy density and (b) cycle life at the current density of 4 A g^{-1}.

Conclusions

The micro–nano structured porous $NiCo_2O_4$ microspheres prepared by spray drying exhibited superior electrochemical properties. Electrochemical tests showed that their specific capacitance was 430.67 and 317.78 F g-1 at current densities of 1 and 10 A g-1, respectively. The $NiCo_2O_4$ electrode has a specific capacitance of 398.22 F g^{-1} after 3000 cycles at 4 A g^{-1} current density, and the capacity retention rate is 100%. Therefore, the micro–nano structured porous spherical $NiCo_2O_4$ powder is a promising candidate for a supercapacitor. On being assembled into an asymmetric supercapacitor, device testing showed specific capacitances of 37.06 F g^{-1} and 20.63 F g^{-1} at current densities of 1 and 10 A g^{-1} and an energy density of 13.18 W h kg^{-1} at a power density of 800 W kg^{-1}. The spherical porous $NiCo_2O_4$ electrode material with a micro–nano structure is beneficial for exhibiting pseudocapacitor characteristics, the diffusion and transfer of charges and an increase in the structural stability and cycle life during the charge–discharge process.

Conflicts of interest

There are no conflicts to declare.

Acknowledgements

The work was financially supported by Natural Science Foundation of Liaoning Province of China (No. 2019-ZD-0122).

References

1 Y. Wang, Z. Q. Shi, Y. Huang, Y. F. Ma, C. Y. Wang, M. M Chen and Y. S. Chen, *J. Mater. Chem.*, 2009, **113**, 13103.
2 L. Wang, J. Yu, X. T. Dong, S. H. Chen, P. Li, H. Q. Hou and Y. H. Song, *ACS Sustainable Chem. Eng.*, 2016, **4**, 1531.
3 R. K. Prataap, R. Arunachalam and R. P. Raj, *Curr. Appl. Phys.*, 2018, **18**, 1143.

4 R. J. Zou, K. B. Xu, T. Wang, G. J. He, Q. Liu, X. J. Liu, Z. Y. Zhang and J. Q. Hu, *J. Mater. Chem. A*, 2013, **30**, 8560.
5 H. L. Wang, Q. M. Gao and L. Jiang, *Small*, 2011, **17**, 2454.
6 G. Q. Zhang and X. W. Lou, *Sci. Rep.*, 2013, **3**, 1470.
7 Q. F. Wang, X. F. Wang, B. Liu, G. Yu, X. J. Hou, D. Chen and G. Z. Shen, *J. Mater. Chem. A*, 2013, **7**, 2468.
8 C. Liu, W. Jiang, F. Hu, F. Wu and D. F. Xue, *Inorg. Chem. Front.*, 2018, **5**, 835.
9 H. W. Wang, Z. A. Hu and Y. Q. Chang, *J. Mater. Chem.*, 2011, **21**, 10504.
10 Y. Zhu, X. Pu, W. Song, Z. Wu, Z. Zhou, X. He, M. Jing, B. Tang and X. Ji, *J. Alloys Compd.*, 2014, **617**, 988.
11 Q. Wang, X. Wang, B. Liu, G. Yu, X. Hou, D. Chen and G. Shen, *J. Mater. Chem. A*, 2013, **1**, 2468.
12 M. Kuang, Y. X. Zhang, T. T. Li, K. F. Li, S. M. Zhang, G. Li and W. Zhang, *J. Power Sources*, 2015, **283**, 270.
13 H. Adhikari, D. Neupane, C. K. Ranaweera, J. Candler, R. K. Gupta, S. Sapkota, X. Shen and S. R. Mishra, *Electrochim. Acta*, 2017, **225**, 514.
14 H. Jiang, J. Ma and C. Z. Li, *Chem. Commun.*, 2012, **48**, 4465.
15 P. Yang, D. Zhao, D. I. Margolese, B. F. Chmelka and G. D. Stucky, *Nature*, 1998, **396**, 152.
16 T. Wang, Y. Guo, B. Zhao, S. Yu, H. P. Yang, D. Lu, X. Z. Fu, R. Sun and C. P. Wong, *J. Power Sources*, 2015, **286**, 371.
17 L. Yu, G. Q. Zhang, C. Q. Yuan and X. W. Lou, *Chem. Commun.*, 2013, **49**, 137.
18 X. Y. Liu, S. J. Shi, Q. Q. Xiong, Y. J. Zhang, H. Tang, C. D. Gu, X. L. Wang and J. P. Tu, *ACS Appl. Mater. Interfaces*, 2013, **17**, 8790.
19 Y. Y. Mi, P. Gao, W. Liu, W. Zhang and H. H. Zhou, *J. Power Sources*, 2014, **267**, 459.
20 X. L. Wu, L. Y. Jiang, F. F. Cao, Y. G. Guo and L. J. Wan, *Adv. Mater.*, 2009, **21**, 2710.
21 S. Wen, G. Li, R. Ren and C. Li, *Mater. Lett.*, 2015, **148**, 130.
22 C. Li, G. Li and X. Guan, *J. Energy Chem.*, 2018, **27**, 923.
23 C. Hu and Y. Lee, *Mater. Chem.*, 1997, **48**, 246.
24 B. Cui, H. Lin, J. B. Li, X. Li, J. Yang and J. Tao, *Adv. Funct. Mater.*, 2008, **18**, 1440.
25 Y. Q. Wu, X. Y. Chen, P. T. Ji and Q. Q. Zhou, *Electrochim. Acta*, 2011, **56**, 7517.
26 Q. Liu, J. Yang, R. Wang, H. Wang and S. Ji, *RSC Adv.*, 2017, **7**, 33635.
27 M. J. Pang, S. Jiang, G. H. Long, Y. Ji, W. Han, B. Wang, X. L. Liu, Y. L. Xi, F. Z. Xu and G. D. Wei, *RSC Adv.*, 2016, **6**, 67839.
28 P. Hao, J. Tian, Y. Sang, C. C. Tuan, G. W. Cui, X. F. Shi, C. P. Wong, B. Tang and H. Liu, *Nano*, 2016, **8**, 16292.
29 X. F. Lu, D. J. Wu, R. Z. Li, Q. Li, S. H. Ye, Y. X. Tong and G. R. Li, *J. Mater. Chem. A*, 2014, **2**, 4706.
30 L. F. Shen, Q. Che, H. S. Li and X. G. Zhang, *Adv. Funct. Mater.*, 2014, **24**, 2630.
31 S. Li, S. Xiong, Y. Liu, Z. Ju and Y. Qian, *ACS Appl. Mater. Interfaces*, 2013, **5**, 981.
32 S. Gao, F. Liao, S. Ma, L. Zhu and M. Shao, *J. Mater. Chem. A*, 2015, **3**, 16520.
33 W. Liu, C. Lu, K. Liang and B. K. Tay, *J. Mater. Chem. A*, 2014, **2**, 5100.
34 A. C. Nwanya, S. U. Offiah, I. C. Amaechi, S. Agbo, S. C. Ezugwu, B. T. Sone, R. U. Osuji, M. Maaza and F. I. Ezema, *Electrochim. Acta*, 2015, **171**, 128.
35 X. Xie, Z. Chang, Y. Tao, W. Lv and Q. H. Yang, *Chem. Commun.*, 2013, **49**, 11092.
36 D. Cai, B. Liu, D. Wang, L. Wang, Y. Liu, H. Li, Y. Wang, Q. Li and T. Wang, *J. Mater. Chem. A*, 2014, **2**, 4954.
37 N. Padmanathan and S. Selladurai, *RSC Adv.*, 2014, **4**, 8341.
38 R. Zhang, H. An, Z. Li, M. F. Shao, J. B. Han and M. Wei, *Chem. Eng. J.*, 2016, **289**, 85.
39 J. L. Liu, L. L. Zhang, H. B. Wu, J. Y. Lin, Z. X. Shen and X. W. Lou, *Energy Environ. Sci.*, 2014, **7**, 3709.